IMMEDIATE COMMUNICATION

# Ucp2-dependent microglia-neuronal coupling controls ventral hippocampal circuit function and anxiety-like behavior

Yuki Yasumoto [1] · Milan Stoiljkovic [1] · Jung Dae Kim[2] · Matija Sestan-Pesa[1] · Xiao-Bing Gao[1] · Sabrina Diano[2] · Tamas L. Horvath[1]

## Abstract

Microglia have been implicated in synapse remodeling by phagocytosis of synaptic elements in the adult brain, but the mechanisms involved in the regulation of this process are ill-defined. By examining microglia-neuronal interaction in the ventral hippocampus, we found a significant reduction in spine synapse number during the light phase of the light/dark cycle accompanied by increased microglia-synapse contacts and an elevated amount of microglial phagocytic inclusions. This was followed by a transient rise in microglial production of reactive oxygen species (ROS) and a concurrent increase in expression of uncoupling protein 2 (*Ucp2*), a regulator of mitochondrial ROS generation. Conditional ablation of *Ucp2* from microglia hindered phasic elimination of spine synapses with consequent accumulations of ROS and lysosome-lipid droplet complexes, which resulted in hippocampal neuronal circuit dysfunctions assessed by electrophysiology, and altered anxiety-like behavior. These observations unmasked a novel and chronotypical interaction between microglia and neurons involved in the control of brain functions.

## Introduction

Research on mechanisms behind cognitive and behavioral disorders has historically focused on the structural and functional abnormalities of neurons. Emerging evidence that non-neuronal brain cells, including microglia, are essential in providing metabolic support, modulation of neurotransmitters release and uptake, and regulation of synapse plasticity have uncovered their active involvement in the etiology of these disorders and proposed novel treatment targets [1]. Microglia, the resident innate immune cells of the brain, have a pivotal role in the clearance of apoptotic cells and neuronal debris, inflammatory response to pathogens or injury, and in surveillance of the local microenvironment. Besides these canonical roles, microglia are important for the remodeling of synaptic connections, an essential process for promoting plasticity and maturation of neural networks during development and adulthood [2]. Specifically, microglia through interaction with neurons, dynamically regulate synapse density by modulation of extracellular matrix and phagocytic elimination of synapse [3, 4]. This property of microglia, once defined as synaptic stripping [5], also serves to maintain the delicate balance between excitation and inhibition in neuronal assemblies, which is particularly important for the regulation of higher brain functions and effective behavioral control. Indeed, the aberrant activity of microglia has been associated with the development of cognitive impairments, depression, and anxiety in several neuropsychiatric disorders and with excessively stressful reactions [6–8]. However, the underpinning mechanism of microglia-mediated synapse remodeling is still not well understood.

Microglial phagocytosis is followed by a rapid increase in the production of reactive oxygen species (ROS), which facilitate phagocytic contents degradation, but at the same

time, may have a detrimental impact on surrounding neurons [9]. Phagocytosis is also an energetically demanding process that requires high adenosine triphosphate (ATP) supply. The generations of both ROS and ATP are closely regulated by mitochondria through adaptations in their molecular architecture and signaling. A molecular intermediate involved in these processes is uncoupling protein 2 (*Ucp2*), a member of the mitochondrial transporter superfamily. *Ucp2* is widely expressed in the brain, including in microglia [10], but its functional relevance in the context of microglia-neuronal interaction is ill-defined. To interrogate this, we used recently generated mice with selective deletion of *Ucp2* in microglia [11]. Here, we particularly focused on the hippocampus given its profound role in cognition and behavior [12], as well as the high immune-vigilant state of microglia therein [13] and extremely intense spine synapse turnover in this structure of the adult brain [14].

## Methods

### Experimental animals

Both male and female, adult microglial specific *Ucp2* knock-out mice (*Ucp2*$^{MGKO}$), and their littermate controls (Ucp2 +/+-Cx3cr1-cre) were used in the study. *Ucp2*$^{MGKO}$ mice were generated by crossing mice expressing tamoxifen-inducible Cre recombinase (CreERT2) in cells expressing CX3CR1 (Cx3cr1-cre: ERT2) and tdTomato reporter (Ai14; cre recombinase-dependent expression) with mice harboring conditional alleles of *Ucp2* (*Ucp2*fl/fl mice) [11]. At the age of 5 weeks, these mice received intraperitoneal injections of tamoxifen (product no. 27190, Cayman Chemical, Ann Arbor, MI) dissolved in corn oil (product No. C8267, Sigma-Aldrich, St. Louis, MO) at a dose of 100 mg/g body weight for 5 consecutive days, and experiments started 4 weeks later to allow the replacement of peripheral monocytes. For performing in vitro electrophysiology experiments, the mice were injected with tamoxifen for 3 consecutive days at the age of 3 weeks. Before being used, animals were housed in a temperature and humidity-controlled room with a 12:12-h light-dark cycle, with a light "on" at 7 a.m.: zeitgeber time (ZT) 0 and "off" at 7 p.m.: ZT12. Animals were provided with free access to food and water at all times. During the study, all measures were taken to minimize the pain or discomfort of the mice. All procedures were performed according to the protocol reviewed and approved by the Yale University Institutional Animal Care and Use Committee and in compliance with the NIH Guide for the Care and Use of Laboratory Animals (NIH Publications no. 80-23, revised 1996).

### Microglia isolation

Microglia were isolated as previously described [11]. Mice were anesthetized and hippocampi were dissociated from the brain and transferred to HBSS buffer. A neural dissociation kit (product No. 130-092-628, Miltenyi Biotec, Waltham, MA) was used to prepare a single-cell suspension, followed by a continuous 30% Percoll gradient at 700 g for 15 min. For microglia/macrophage isolation, cells were incubated with biotin-conjugated anti-CD11b antibody (eBioscience product no. 13-0112-82, Thermo Fisher Scientific, Waltham, MA), and CD11b + cells were isolated using Dynabeads Biotin Binder (Invitrogen product no. 11047, Thermo Fisher Scientific) and following manufacturer's instruction.

### RNA preparation and qPCR

Total RNA was extracted from chopped and homogenized hippocampi, and isolated microglia/macrophage (CD11b+ cells) using RNeasy Plus Mini kit (product no. 74134, Qiagen, Germantown, MD). cDNA synthesis was performed using QuantiTect Reverse Transcription Kit (product no. 205311, Qiagen). qPCR with diluted cDNAs was performed using the LightCycler 480 (Roche Diagnostics, Mannheim Germany) and Taqman Gene Expression Assay primers (Thermo Fisher Scientific) in duplicates. Gene expression of the target genes was normalized to b-actin. Quantification was performed by normalizing Ct (cycle threshold) values to GAPDH and was analyzed by the comparative Ct method with the Roche LightCycler 480 software. The following Primers were used: Cx3cr1, Mm02620111_s1; Ucp2, Mm00627599_m1; b-Actin, Mm02619580.

### Measurement of mitochondria oxidation (ROS) in vivo

In vivo mitochondrial ROS production in immunostained microglia was measured by injecting dihydroethidium (DHE; Invitrogen product no. D11347, Thermo Fisher Scientific), as it is specifically oxidized by superoxide to red fluorescent ethidium. A 1 mg/ml concentration was injected into the retro-orbital sinus of lightly anesthetized mice and mice were transcardially perfused 3 h later.

### Perfusion and tissue processing

Mice were anesthetized and transcardially perfused with 0.9% saline followed by fixative (4% paraformaldehyde, 15% picric acid, 0.1% glutaraldehyde in 0.1 M phosphate buffer (PB; pH 7.4)). Brains were removed and postfixed in the same fixative without glutaraldehyde for 48 h at 4 °C

and then stored in 0.1 M PB. Coronal 50 μm sections were cut on a PELCO easiSlicer vibratome (Ted Pella, Inc., Redding, CA) and followed by immunohistochemistry and EM analysis.

## Electron microscopy analysis

Free-floating sections (50 μm thick) were incubated with anti-Iba1 antibody diluted 1:3000 in 0.1 M PB (product No. 019-19741, Wako Pure Chemical Industries, Ltd., Osaka, Japan) after 1 h blocking in 0.1 M PB with 5% normal goat serum. After several washes with PB, sections were incubated in the secondary antibody (biotinylated goat anti-rabbit IgG; 1:250 in PB; Vector Laboratories Inc., Burlingame, CA) for 2 h at room temperature, then rinsed in PB three times 10 min each time, and incubated for 2 h at room temperature with avidin–biotin–peroxidase (ABC; 1:250 in PB; VECTASTAIN Elite ABC kit PK6100, Vector Laboratories). The immunoreaction was visualized with 3,3-diaminobenzidine (DAB). Sections were then osmicated (1% osmium tetroxide) for 30 min, dehydrated through increasing ethanol concentrations (using 1% uranyl acetate in the 70% ethanol for 30 min), and flat-embedded in Araldite between liquid release-coated slides (product no. 70880, Electron Microscopy Sciences, Hatfield, PA). After embedding in Durcupan (product no. 14040, Electron Microscopy Sciences), ultrathin sections were cut on a Leica Ultra-Microtome, collected on Formvar-coated single-slot grids, and analyzed with a Tecnai 12 Biotwin electron microscope (FEI). To evaluate the ultrastructure within hippocampus stratum radiatum, 10–30 images were taken per mouse. Synapse count was performed following the protocol by Diano et al. [15] with modifications (expressed as the number of synapses per 100 μm$^2$). ImageJ was used to measure microglial process-synapse contact, phagocytic inclusion coverage, lysosome, and lipid droplet (LD) coverage (expressed as the number per process, percentage of the area to process, or cytosol area).

## Immunohistochemistry analysis

Free-floating sections (50 μm-thickness) were treated with 0.3% Triton X-100/ PBS. After the sections were blocked in 5% donkey serum, they were incubated with the following primary antibodies for 48 h at 4 °C: rabbit anti-Iba1 antibody, 1:2000 (Wako Pure Chemical Industries, Ltd.) and rat anti-CD68, 1:200 (product No. MCA1957, Bio-Rad Laboratories, Inc., Hercules, CA). The sections were then incubated with the following secondary antibodies for 3 h at room temperature: anti-rabbit IgG-Alexa488 and anti-rat IgG-Alexa488 (1:1000 for both; Invitrogen). Sections were mounted on microscope slides and embedded with Vectashield that includes DAPI for nuclear staining (product no.

H-1200, Vector Laboratories, Inc). Three or four Images of vCA1 per mouse were obtained randomly using a confocal microscope (model Zeiss LSM880 Airy Scan). A series of sections were obtained at 1.0 μm increments along the Z-axis of the tissue section at 20× magnification. The maximum intensity projections (MIP) of the consecutive optical slices were made using Zen software (Carl Zeiss Microscopy LLC., White Plains, NY). ImageJ (https://imagej.nih.gov/ij) was used for quantification of DHE and CD68 positive area in Iba1 or tomato positive microglia and compared between control and $Ucp2^{MGKO}$ mice.

## In vivo electrophysiology

Local field potentials (LFPs) recordings were carried out between ZT0 and ZT6 in mice anesthetized with urethane (1.5 g/kg) given intraperitoneally. After achieving a stable plane of anesthesia, which was confirmed by the absence of a tail-pinch reflex, mice were placed in a Kopf stereotaxic frame (Tujunga, CA) on a temperature-regulated heating pad (Physitemp Instruments Inc., Clifton, NJ) set to maintain body temperature at 37–38 °C, and unilateral craniotomies were performed above the hippocampus. After surgery, bipolar concentric stainless steel recording electrodes (NE-100X, Rhodes Medical Instruments, Woodland Hills, CA) were inserted into the dorsal and ventral aspect of the hippocampal CA1 region, and animals were allowed to stabilize for 30 min before the beginning of LFPs recordings. Coordinates for positioning electrodes were taken from mouse stereotaxic brain atlas [16] and referenced relative to bregma and brain surface (dorsal CA1 (dCA1): 2.0 mm posterior, 1.5 mm lateral and 1.5 mm dorsoventral, and ventral CA1 (vCa1): 3.4 mm posterior, 3.5 mm lateral, and 3.5 mm dorsoventral). Throughout the duration of the experiment, mice were kept in the stereotaxic frame, spontaneous LFPs were continuously monitored, and the level of anesthesia regularly checked. After all recordings, animals were deeply anesthetized, transcardially perfused, and their brains removed for histological analysis.

In each experiment, LFPs were amplified and filtered between 1 and 300 Hz using Grass P55 AC differential amplifier (Grass Technologies, West Warwick, RI) with an additional notch filter at 60 Hz. The signal was simultaneously sampled at a rate of 1 kHz and stored on a computer via a CED Micro1401–3 interface and Spike2 software (Cambridge Electronic Design, Cambridge, UK). For quantitative offline analyses of LFPs power, the signal was subjected to Fast Fourier transform (FFT) at a spectral resolution of 0.24 Hz. Power analyses during the spontaneous hippocampal activity were performed using 10-min long epochs by summing FFTs in theta (4–9 Hz), and gamma (30–90 Hz) frequency range. For gamma power

computation, the LFPs signal was first band-pass filtered between 30 Hz and 90 Hz. In a subset of mice effect of N-methyl-D-aspartate receptors (NMDA) blockade on gamma oscillation in vCA1 was tested. After recording of stable baseline for at least 30 min, mice were subcutaneously injected with 0.5 mg/kg MK-801 (Tocris Bioscience, Bristol, UK) and LFPs followed for an additional 60 min. Drug-induced changes in gamma power were calculated as the percent change from baseline power in every animal over 10 min post-treatment interval, starting 30 min following injection.

## In vitro electrophysiology

Control and $Ucp2^{MGKO}$ mice were deeply anesthetized with isoflurane and decapitated, their brains rapidly removed, trimmed to a tissue block containing only the cortex and hippocampus. Coronal tissue sections of 300 μm thickness were made using vibratome in an oxygenated (5% $CO_2$ + 95% $O_2$) cutting solution at 4 °C containing (in mM): sucrose 220, KCl 2.5, $CaCl_2$ 1, $MgCl_2$ 6, $NaH_2PO_4$ 1.25, $NaHCO_3$ 26, and glucose 10, pH 7.3 with NaOH. After preparation, slices trimmed to contain only the hippocampus were maintained in a storage chamber with oxygenated artificial cerebrospinal fluid (ACSF) containing (in mM): NaCl 124, KCl 3, $CaCl_2$ 2, $MgCl_2$ 2, $NaH_2PO_4$ 1.23, $NaHCO_3$ 26, glucose 10, pH 7.4 with NaOH. Hippocampal slices were transferred to a recording chamber constantly perfused with ACSF at 33 °C with a rate of 2 ml/min after at least an hour of recovery. Whole-cell voltage-clamp (at −60 mV or at 0 mV) was performed as described previously [17] to observe miniature excitatory and inhibitory post-synaptic currents (mEPSC and mIPSC) using Multiclamp 700 A amplifier (Axon Instruments, Molecular Devices, LLC. San Jose, CA). The patch pipettes with a tip resistance of 4–6 MΩ were made of borosilicate glass (World Precision Instruments, Sarasota, FL) with a Sutter pipette puller (P-97) and filled with a pipette solution containing (in mM): K-gluconate 135, $MgCl_2$ 2, HEPES 10, EGTA 1.1, Mg-ATP 2, $Na_2$-phosphocreatine 10, and $Na_2$-GTP 0.3, pH 7.3 with KOH. After the giga-ohm (GΩ) seal and whole-cell access were achieved, the series resistance (10–20 MΩ) was partially compensated by the amplifier. All data were sampled at 10 kHz and filtered at 3 kHz with an Apple Macintosh computer using AxoGraph X (AxoGraph, Inc). Data were analyzed using an event-detection package in AxoGraph X and plotted with Igor Pro software (WaveMetrics, Lake Oswego, OR).

## Behavioral tests

All behavior tests were performed in a dimly lit room between ZT0 and ZT6 and tracked with Any-Maze software

(Stoelting Co., Wood Dale, IL). For acclimation, mice were transferred to the examination room at least 1 h prior to the tests.

## Elevated zero maze

Anxiety-like behavior was assessed using an elevated zero maze [18] consisted of a ring-shaped platform, 60 cm in diameter, 4.3 cm wide, and elevated 52 cm above the floor. The maze was divided into four equal quadrants, two opposing arms were enclosed by 15.5 cm high gray walls whereas the other two were opened. Each mouse was placed in the center of an open arm and allowed to explore the platform for 5 min. Mouse behavior was recorded with an overhead video camera connected with the ANY-maze software for measuring the time spent and distance traveled in the open arm.

## Open field test

The open-field test was performed to measure exploratory behavior, general activity, and fear [19]. Mice were placed in the center of an open field (37 cm × 37 cm × 30 cm) and allowed to explore the field for 10 min. The open field was divided into three zones, peripheral, intermediate, and center zone. During a mouse's exploration of the field, tracking of total distance traveled, and total time traveled were recorded with a video camera connected to ANY-maze tracer software.

## Novel object recognition test

The novel object recognition test was used to assess recognition memory [20, 21]. Experiments were performed 24 h after habituation to an open field (37 cm × 37 cm × 30 cm) when each mouse was presented with two exact same objects (Falcon tissue culture flasks filled with corn-based animal bedding (10 cm high, 2.5 cm deep and 5.5 cm wide, transparent plastic with a blue bottle cap)) in the field and allowed to explore for 10 min. After a short intersession interval (2 h), each mouse was placed back to the same box, where one of the two familiar objects was switched to a new one (towers of Lego bricks (10 cm high and 5.8 cm wide, built-in blue, yellow, red, purple and green bricks)). Mouse behavior was recorded with an overhead video camera connected to ANY-maze. The amount of time taken to explore the new object was measured by the ANY-maze software and the novel preference and the discrimination index percentage were calculated as follows: novel preference (%) = (time exploring novel object/time exploring novel object + time exploring familiar object) × 100; and discrimination index (%) = (time exploring novel object − time exploring
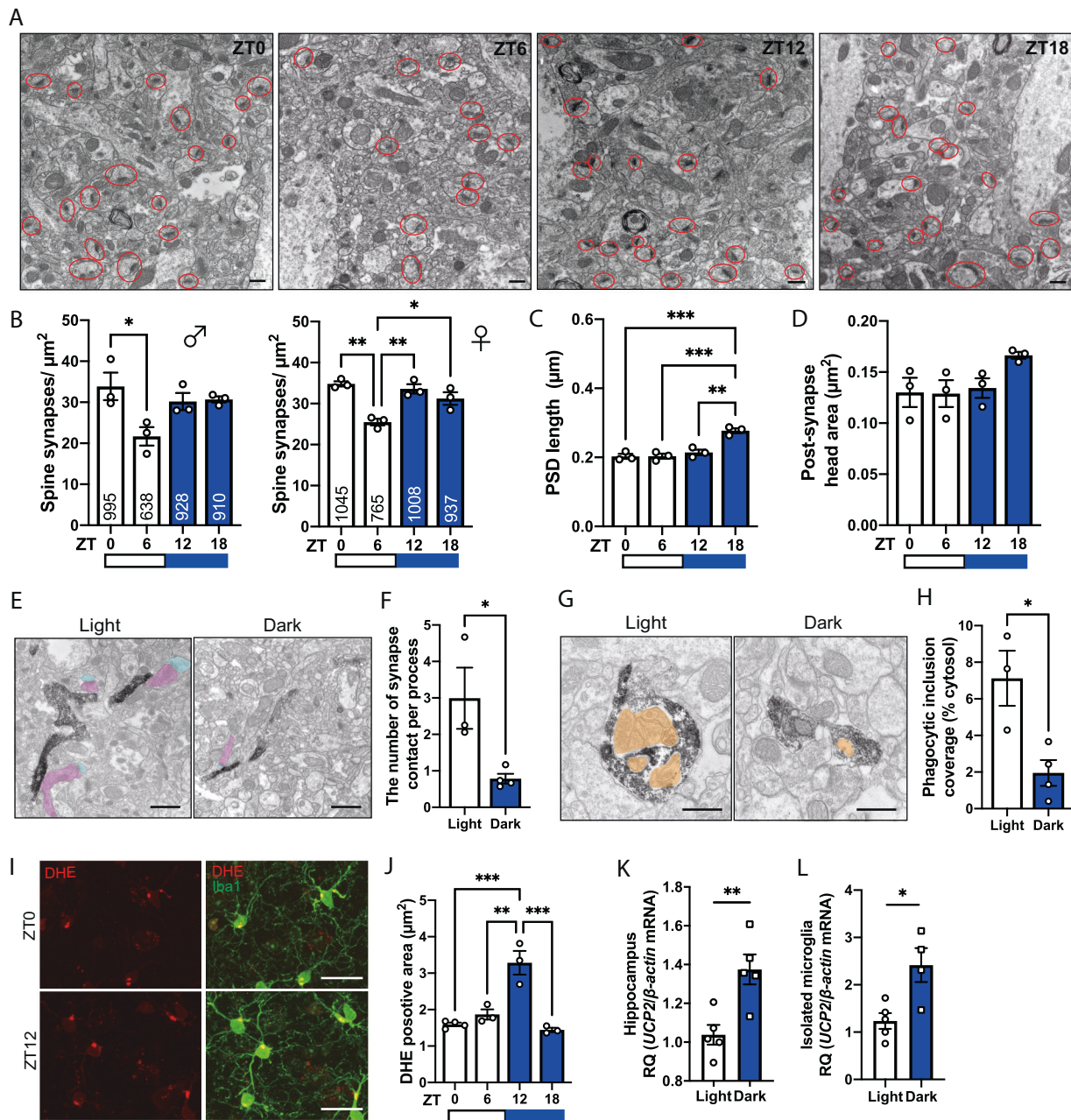
**Fig. 1 Chronotypical pattern of microglia-controlled spine synapse number and morphological alterations in vCA1 region.**
**A–D** Representative electron microscopic images of spine synapses (encircled in red) in stratum radiatum layer of vCA1 of male mice at zeitgeber times ZT0, ZT6, ZT12, and ZT18 (**A**). Dynamic changes of synapse number (left: male, right: female, the total number of synapses from three mice are listed in each bar) (**B**). Postsynaptic density (PSD) length (**C**), and postsynaptic head area (**D**) at ZT0, ZT6, ZT12, and ZT18 estimated by measuring 135 synapses of male mice. **E–H** Representative electron microscopic images and quantification of microglia-synapse contacts per process (**E**) and (**F**), and phagocytic inclusion coverage (**G**) and (**H**) at light (left) and dark (right) phase. Immunostained Iba1 sections showing presynaptic (pink), postsynaptic (blue) compartments, and phagocytic inclusions (orange). **I, J** Representative confocal images of DHE + (red) and Iba1 + (green) at ZT0 and ZT12 (**I**), and quantification of DHE + area in Iba1 immunoreactive microglia (**J**). **K, L** Quantitative PCR analyses of relative *Ucp2* mRNA expression in the bulk of hippocampus (**K**) and isolated hippocampal microglia (**L**) at light/dark phase (**K**) and (**L**). Data are presented as histograms with individual values ± s.e.m from $n = 3$ (**B**) and (**D**), $n = 3$–4 (**F**), (**H**), and (**J**), $n = 5$ (**K**) and (**L**) mice/group all synapse count and morphology estimation analyses were independently repeated once for double comparisons and similar results obtained. *$p < 0.05$; **$p < 0.01$; ***$p < 0.001$, by one-way ANOVA with Tukey's post hoc test (**B**)–(**D**) and (**J**) or two-tailed Student's *t*-test (**F**), (**H**), (**K**), and (**L**). Scale bars, 500 nm (**A**), (**E**), and (**G**), 20 μm (**I**).

familiar object)/(time exploring novel object + time exploring familiar object) × 100.

## Marble burying test

The marble-burying test was employed to assess compulsive-like behaviors [22]. The cages were filled with 5 cm of corn-based animal bedding. Twenty-four glass marbles were evenly placed on the surface and leave each mouse for 30 min. The number of marbles buried more than 2/3 their depth with bedding was counted.

## Y maze

Spatial short-term memory was assessed using the Y maze as described previously [23]. The Y maze apparatus has three arms (30 cm × 30 cm × 30 cm), 8 cm lane width, and 15 cm wall height at 120° angle from each other. Each mouse was placed at the end of one arm facing the center and allowed to freely explore the three arms for 10 min. The number and the sequence of arms entered were recorded with an overhead video camera connected to ANY-maze. The number of alternations was defined as consecutive entries into each of the three different arms without repetition. The percentage of alternation was calculated as the following quotient: the number of alternations/(total arm entries − 2) × 100.

## Statistical analysis

All data were initially determined to be suitable for parametric analysis according to normality and homoscedasticity. Statistical difference was assessed using one-way ANOVA or two-way ANOVA with Tukey's post hoc test and two-tailed Student's $t$-test (GraphPad Prism Software, Inc., La Jolla, CA). Differences were considered significant when $p < 0.05$.

# Results

## Spine synapse number and morphology are regulated in a chronotypical manner in the ventral hippocampal CA1 region

First, we found that microglia-mediated spine synapse elimination in the hippocampus exhibits a chronotypical pattern with a higher propensity for synaptic phagocytosis during the light phase. Electron microscopic (EM) analyses revealed a significant decrease in the number of spine synapses in the stratum radiatum of the ventral hippocampal CA1 region (vCA1) of male mice at ZT6 (middle of the light phase) comparing to ZT0 (end of the dark phase),

($F_{(3,8)} = 5.07$, $P = 0.030$) (Fig. 1A, B: left graph). A similar pattern was observed in female mice ($F_{(3,8)} = 14.60$, $P = 0.001$) (Fig. 1B: right graph), where differences were also found comparing with the other two time points. In contrast, analyses of synaptic morphological features revealed significantly greater length ($F_{(3,8)} = 23.20$, $P < 0.001$) of postsynaptic density (PSD) only at ZT18 (middle of the dark phase), whereas the other synaptic elements such as postsynaptic head area, diameter, and length were not changed in these synapses across measured ZT points (Fig. 1A, C, D, Supplementary Table 1).

## Chronotypically regulated microglial synaptic pruning induced ROS production and Ucp2 expression

Next, to assess microglial engulfment activity, we quantified microglia-synapse contacts per process and relative phagocytic inclusion coverage by EM. We found a significantly increased contact number ($t = 3.07$, df = 5, $P = 0.028$) and inclusion area ($t = 3.43$, df = 5, $P = 0.019$) during the light phase (Fig. 1E–H). Further, we detected a rise in microglial ROS production peaking at ZT12 (end of the light phase) ($F_{(3,9)} = 24.59$, $P < 0.001$) (Fig. 1I, J), followed by subsequent upregulation of *Ucp2* mRNA expression in the bulk hippocampus (Fig. 1K), and in isolated hippocampal microglia (Fig. 1L) during the dark phase ($t = 3.66$, df = 8, $P = 0.006$; $t = 3.22$, df = 7, $P = 0.015$, respectively). When comparing *Ucp2* mRNA level in isolated hippocampal microglia between sexes, a higher level in female mice was found ($t = 3.53$, df = 4, $P = 0.024$) (Supplemental Fig. 1A). Together, these results indicate that microglia are actively involved in synapse remodeling in vCA1 of mice during their daylight dormancy and this process is accompanied by increased ROS and *Ucp2* levels.

## Loss of Ucp2 in microglia leads to increased ROS production and aberrant phagocytic phenotype

To further determine *Ucp2* functional role in the regulation of microglial phagocytosis-mediated synapse remodeling and plasticity in the hippocampus, we used *Ucp2*MGKO mice with microglial specific ablation of *Ucp2* [11]. In these mice, we found that hippocampi-derived microglia (CD11b-positive cells) had a 91 ± 4 % decrease in *Ucp2* mRNA level compared to microglia from control mice after 4 weeks from tamoxifen treatment (Supplementary Fig. 1B). No difference in hippocampal *Ucp2* mRNA levels was observed in CD11b-negative cells, i.e., non-microglial cells, between control and *Ucp2*MGKO mice (Supplementary Fig. 1C). Importantly, in these CD11b-negative cells expression of *Cx3cr1* mRNA was barely detectable comparing to CD11b-positive cells (Supplemental Fig. 1D),
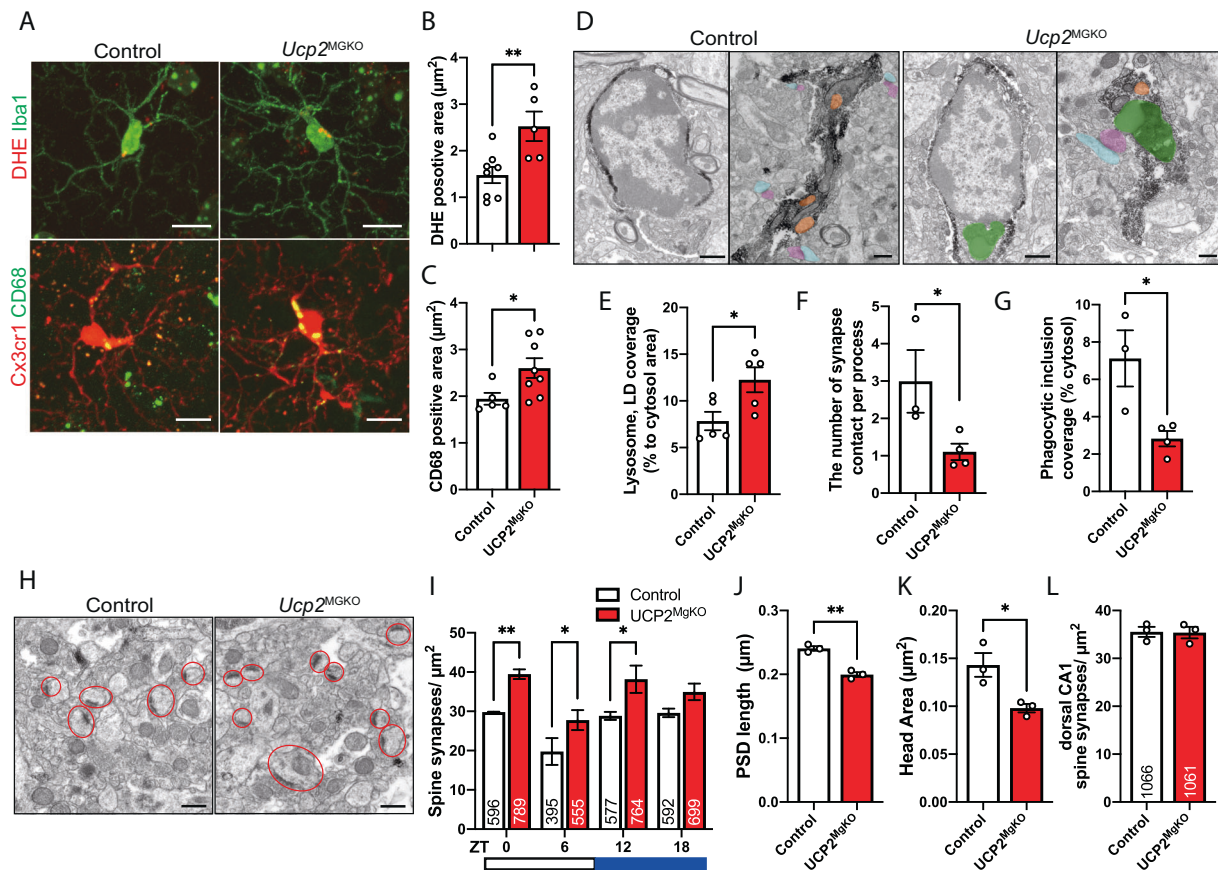
**Fig. 2 Alteration of microglial ROS production, phagocytosis, and synapse number in vCA1 region by microglia selective Ucp2 deletion. A–C** Representative confocal images showing DHE probes (red) and Iba1 staining (green) of control (left) and $Ucp2^{MGKO}$ (right) male mice ((**A**), upper panels), and tomato-expressing microglia (red) and CD68 staining (green) ((**A**), lower panels). Quantification of DHE+ area in Iba1 immunoreactive microglia (**B**) and CD68 + area (**C**). **D–G** Representative electron microscopic images of Iba1-immunostained microglial cell body (upper panels) and process (lower panels) of control (left) and $Ucp2^{MGKO}$ (right) male mice (**D**). Quantification of lysosomal and lipid droplet coverage (**E**), number of synapse contact per microglial process (**F**), and phagocytic inclusion area (**G**). **H–K** Representative electron microscopic images of spine synapses (encircled in red) in stratum radiatum layer of vCA1 of control (left) and $Ucp2^{MGKO}$ (right) male mice at ZT0 (**H**) with spine synapse counts (**I**). PSD length (**J**) and postsynaptic head area (**K**) estimated by measuring 135 synapses. **L** Spine synapse number in dCA1 of male control and $Ucp2^{MGKO}$ mice. Data are presented as histograms with individual values ± s.e.m. ($n = 3$–8 mice/group, 5–10 images per animal) (**B**), (**C**), (**E**), (**G**), (**I**)–(**L**). The total number of synapses from two mice per genotype is listed in bar graphs (**B**). All synapse count and morphology estimation analyses were independently repeated once for double comparisons and similar results obtained. *$p < 0.05$; **$p < 0.01$, by two-way ANOVA with Tukey's post hoc test (**I**), or two-tailed Student's t-test (**B**), (**C**), (**E**)–(**G**), (**J**)–(**L**). Scale bars, 10 μm (**A**), 500 nm (**D**), and (**H**).

which validates microglial isolation protocol. To detect the ROS level in these mice, dihydroethidium (DHE) was injected intravenously and DHE positive area quantified. In addition, we used CD68, a marker of the lysosome, to quantify lysosome accumulation. We found significantly increased ROS level ($t = 3.18$, df = 11, $P = 0.009$) and accumulation of lysosomes ($t = 2.28$, df = 11, $P = 0.044$) in microglia of hippocampal vCA1 compared to their controls at ZT12 (Fig. 2A, B). Moreover, mutant mice had larger lysosomal vacuoles and a higher number of LDs covering a sizeable portion of the microglial cell body and processes ($t = 2.67$, df = 8, $P = 0.028$) in EM analyses (Fig. 2D, E). Also, these mice showed significantly fewer synapse contacts ($t = 2.52$, df = 5, $P = 0.049$), and phagocytic

inclusions ($t = 3.18$, df = 5, $P = 0.024$) in microglial processes comparing to controls (Fig. 2F, G).

## Microglial specific Ucp2 deletion induced an increase in synapse number in the ventral hippocampal CA1 region

As a consequence, $Ucp2^{MGKO}$ mice had a remarkably higher number of spine synapses in the stratum radiatum of vCA1 measured over ZT0-ZT12 periods ($F_{(1,8)} = 54.35$, $P < 0.001$) (Fig. 2H, I). However, temporal dynamics of synapse elimination therein were still preserved ($F_{(3,8)} = 20.41$, $P < 0.001$) (Fig. 2I). By examining synapse morphology in $Ucp2^{MGKO}$ mice we detected shorter PSD length

($t = 8.11$, df = 4, $P < 0.01$) and smaller post-synapse area ($t = 3.43$, df = 4, $P = 0.027$) than in control littermates (Fig. 2J, K). Importantly, these synapse alterations were not observed in the dorsal CA1 region (dCA1) of $Ucp2^{MGKO}$ mice (Fig. 2L), suggesting that $Ucp2$ may play a role in the region-specific function of microglia within the hippocampus and brain.

## Microglial specific Ucp2 deletion altered neurophysiological functions

To interrogate the effect of $Ucp2$-dependent alterations of microglial synapse remodeling on hippocampal circuit integrity we performed both in vivo and in vitro electrophysiological recordings from male and female $Ucp2^{MGKO}$ and control mice. Recordings of LFPs from the vCA1 in anesthetized $Ucp2^{MGKO}$ male mice revealed a significant reduction in gamma oscillation power ($t = 2.61$, df = 12, $P = 0.029$) and suggestive decline in theta oscillation power ($t = 1.81$, df = 10, $P = 0.099$) (Fig. 3A–C). In contrast, changes in these oscillatory bands were not found in dCA1 of male $Ucp2^{MGKO}$ mice comparing to their control counterparts (Fig. 3F–H). In addition, female $Ucp2^{MGKO}$ mice also showed similar results as controls for hippocampal gamma and theta power in both vCA1 and dCA1 recordings (Fig. 3D, E, I, J). Treatment with MK-801, a noncompetitive antagonist of glutamatergic NMDA receptors, was able to rescue altered gamma oscillation in male mice since the comparable increase in vCA1 gamma power was observed in both mutant and control animals ($t = 1.04$, df = 4, $P = 0.359$) (Fig. 3K). In the further characterization of neuronal alteration observed in vCA1, we performed whole-cell voltage-clamp recordings in hippocampal slices and compared miniature excitatory/inhibitory postsynaptic currents (mEPSC/mIPSC) in male $Ucp2^{MGKO}$ and control mice. We found a significantly higher frequency of mIPSC in $Ucp2^{MGKO}$ ($t = 2.24$, df = 25, $P = 0.035$) (Fig. 3L, M), which confirmed functional impairment of neuronal activity in vCA1 of these mice.

## Microglial specific Ucp2 deletion evoked anxiety-like behavior

Finally, behavioral testing of $Ucp2^{MGKO}$ mice revealed increased anxiety levels. In the elevated zero maze test, male mutant mice spent significantly less time ($t = 2.50$, df = 17, $P = 0.023$) (Fig. 4A) and had shorter distance traveled ($t = 2.11$, df = 17, $P = 0.050$) (Fig. 4B) in the stressful open arms as compared to their controls. In contrast, this anxiety-like phenotype was not observed in female mice (Fig. 4A, B). Interestingly, testing these mice in the open field did not reveal a marked difference in locomotor activity between $Ucp2^{MGKO}$ and controls of either gender (Fig. 4C), but, consistent with the results in the elevated zero maze, male $Ucp2^{MGKO}$ mice had a tendency to stay shorter in the center zone of the open field arena (Fig. 4D, E). Moreover, when comparing the performance of $Ucp2^{MGKO}$ and control animals of either gender in novel object recognition (Fig. 4F, G), marble burying (Fig. 4H), and Y-maze tasks (Fig. 4I) no obvious alteration has been detected.

## Discussion

In the healthy adult brain, microglia-neuronal interaction is believed to have a prominent role in securing the permanence of neuronal activity in the optimal range, thereby providing homeostatic control of network function and behavior. Here, we show that this interaction in the mouse ventral hippocampus operates in the chronotypical pattern with microglia active phagocytic pruning of synapses during the light phase. We provide evidence that this process critically depends on mitochondrial protein $Ucp2$ since ablation of $Ucp2$ in microglia hindered synapse elimination triggering changes in hippocampal circuit function and inducing anxiety-like behavior.

Alternating environmental states of day and night are considered among the strongest salient stimuli capable to entrain changes in neuronal structure and function that confer synaptic plasticity [24]. In the hippocampus, the magnitude of plasticity in the CA1 region is regulated in a time-dependent manner, and this may help prevent saturation of long-term potentiation/depression, and the hyperstimulation of local networks, thereby limiting their negative impact on cognition and neuronal health [25]. These important aspects of homeostasis are partly gated by circadian rhythm-driven expression of hippocampal clock gene [24], but other mechanisms including microglial activation as we observed may also have substantial involvement. In support of the latter, we found that synapse phagocytosis in vCA1 is followed by a rise in microglial ROS production which is known to enable phagocytic clearance. However, at the same time, ROS excessive formation can cause cell damage and reduce engulfment capacity. Previous evidence showed that $Ucp2$ can toggle ROS level protecting cells from excessive ROS formation [9, 26]. Consistently, we detected a significant increase of $Ucp2$ both in the hippocampus and isolated hippocampal microglia during the dark phase, after the peak of ROS production.

In peripheral macrophages, $Ucp2$ is a major molecular determinant that mediates mitochondrial function during phagocytosis [26]. Recently we provided evidence that $Ucp2$-dependent mitochondrial changes contribute to microglial activation and neuroinflammation induced by a
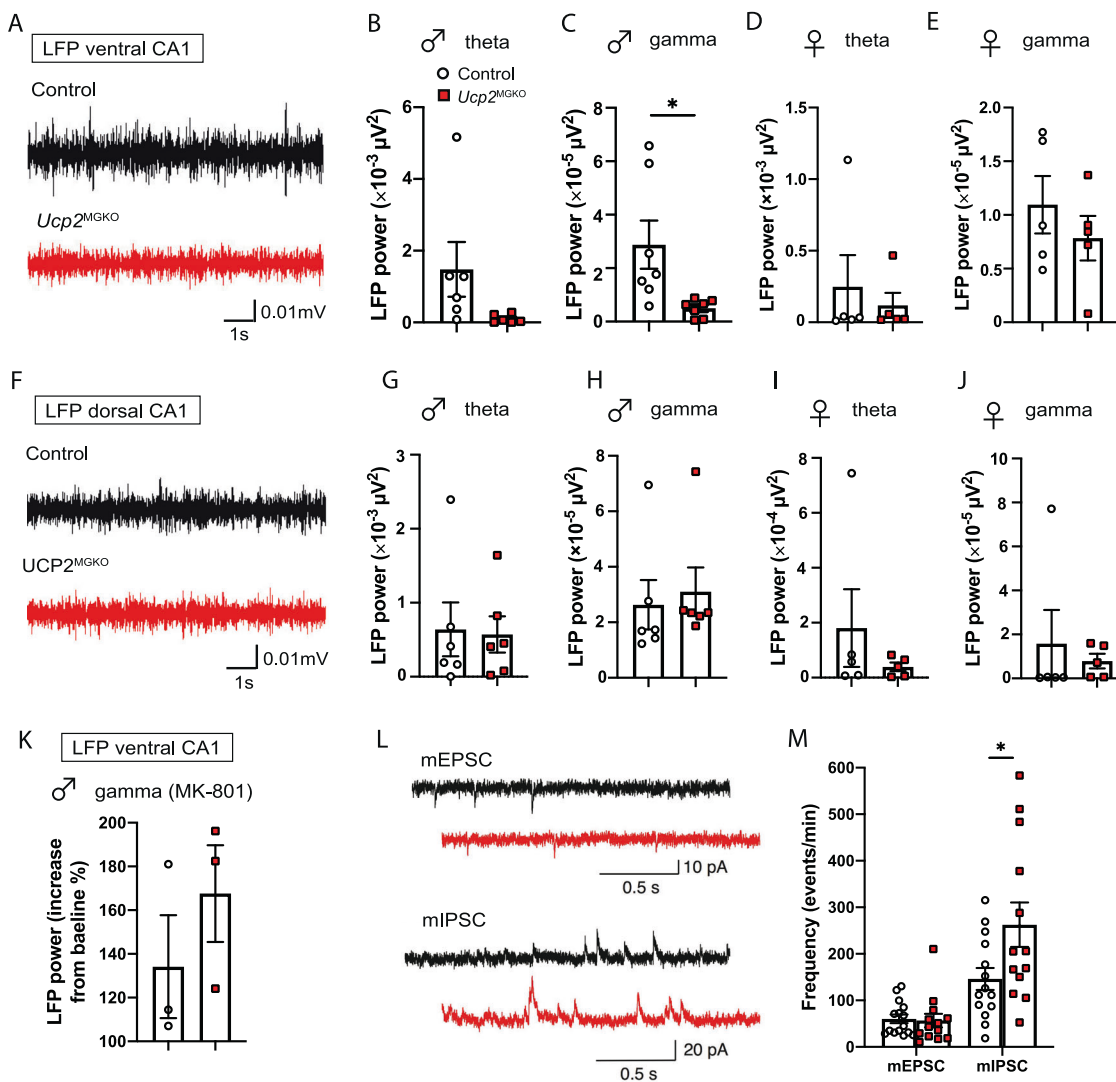
**Fig. 3 Differential neurophysiologic characteristics of hippocampal vCA1 and dCA1 in *Ucp2^{MGKO}* mice. A–K** Typical traces of spontaneous local field potentials (LFPs) in gamma frequency range from control (black) and *Ucp2^{MGKO}* (red) male mice recorded in vivo from vCA1 (**A**) and dCA1 region (**F**). Both signals are digitally band-pass filtered between 30 and 90 Hz (**A**) and (**F**). Power of theta (4–9 Hz) ((**B**), (**G**), male, (**D**), (**I**), female), and gamma (30–90 Hz) ((**C**), (**H**), male, (**E**), (**J**), female) band oscillations. Relative change in gamma power following MK-801 (0.5 mg/kg) subcutaneous injection (**K**). **L, M** Representative traces of miniature excitatory postsynaptic current (mEPSC, upper panel) and miniature inhibitory postsynaptic current (mIPSC, lower panel) from control (black) and *Ucp2^{MGKO}* (red) mice acquired from whole-cell recordings in vCA1 (**L**), and a corresponding analysis of spontaneous mEPSC and mIPSC frequency of occurrence (**M**). Data are presented as histograms with individual values and s.e.m. ($n = 5$–7 mice/group for (**B**)–(**E**) and (**G**)–(**J**); $n = 3$ mice/group for (**K**) and 13–15 cells/3 mice for (**M**)). *$p < 0.05$, by two-tailed Student's *t*-test.

high-fat diet [11]. In the current study, we show that microglial *Ucp2* plays an important role in the lysosomal-autophagy pathway since the analysis of *Ucp2^{MGKO}* mice lacking microglial *Ucp2* revealed both significant increases in ROS and defective lysosomal degradation of LDs. It has been suggested that accumulated LDs in microglia contribute to impairment of cellular energy metabolism given the shortage in free fatty acids for mitochondrial β-oxidation and generation of ATP provided by their degradation [27]. Moreover, LDs themselves may induce inflammation and sequestration of lysosomes compromising their role in phagocytosis as shown for the hippocampal microglia after lipopolysaccharide treatment or during aging [27]. Both of these effects could propel into further microglial dysfunctions. Accordingly, *Ucp2*-driven substantial transformation of microglia in *Ucp2^{MGKO}* mice resulted in suppression of spine synapse remodeling that yields to alteration in hippocampal circuit function and related behavior.

In vivo recordings of LFPs revealed a reduction in gamma oscillation power in vCA1 of *Ucp2^{MGKO}* male mice, without marked changes in activity in dCA1 or in the hippocampus of female knock-out mice. It is well-established
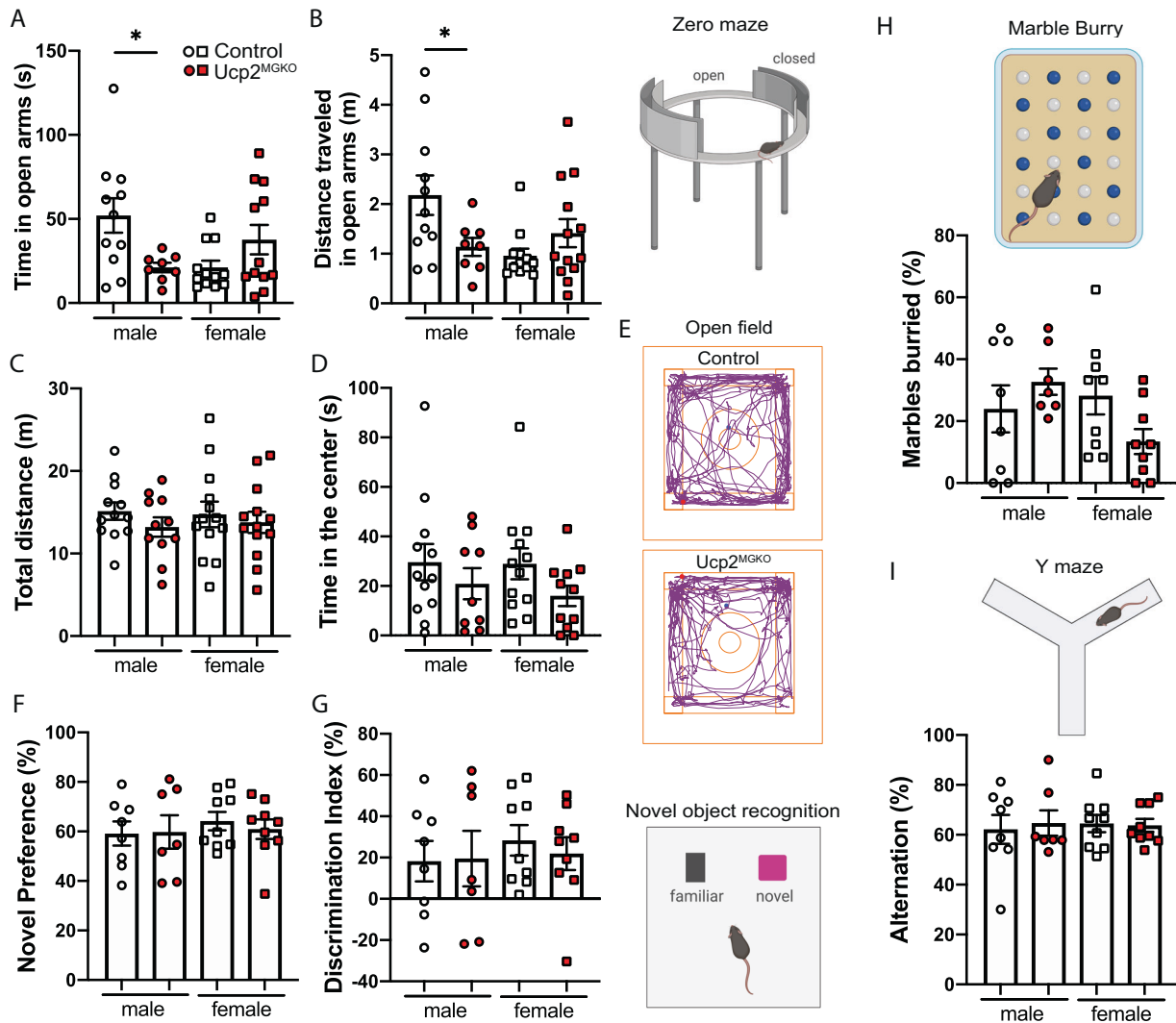
**Fig. 4 Development of anxiety-like behavior in *Ucp2^{MGKO}* male mice.** Behaviors of male and female control and *Ucp2^{MGKO}* mice were examined by multiple assays. **A**, **B** Elevated zero maze test. **C–E** Open field test. **F**, **G** Novel object recognition test. **H** Marble burry and (**I**), Y maze test. Time spent (**A**) and distance traveled (**B**) in open arms in elevated zero mazes. Total distance traveled (**C**), time spent in the center zone (**D**), and representative tracking of control ((**E**), upper panel) and *Ucp2^{MGKO}* ((**E**), lower panel) mouse in the open field. Novel object preference (**F**) and discrimination index (**G**), percentage of marbles buried (**H**), and spontaneous alternation in *Y* maze (**I**). Data are presented as histograms with individual values and s.e.m. ($n =$ 8–12 mice/group for all teats). $*p < 0.05$, by two-tailed Student's *t*-test.

that network oscillations depend on the integrity of the synaptic contacts and precise temporal synchronization of neural activity in local circuits [28]. Furthermore, high-frequency oscillation phenomena, such as gamma (30–90 Hz), greatly rely on fine-tuning of excitation and inhibition between pyramidal cells and interneurons [29]. Given that spine synapses closely correspond to the excitatory synapses [30], their increase in number as found in *Ucp2^{MGKO}* mice can induce an excitatory gain in the local vCA1 circuitry which offset the excitatory/inhibitory balance. This results in the asynchronous firing of pyramidal neurons reflected as a decrease in oscillation power. In the hippocampal network during the gamma cycle, phasic glutamate excitatory inputs from pyramidal neurons, via feedback loop drive parvalbumin-positive (PV+) interneurons to fire with a delay due to the monosynaptic nature of recurrent connections [29]. Since gamma oscillation critically depends on synchronous activation of inhibitory fast-firing PV+ interneurons, increasing excitation in synapses onto these cells, which can be long-lasting in case of glutamate NMDA mediated-currents, prompts PV+ interneurons to generate action potentials that are not locked to the excitatory discharge from the pyramidal cells inducing firing desynchronization in the network. In agreement, a computational model network of reciprocally connected pyramidal cells and interneurons demonstrated that increasing NMDA tone decrease gamma power, suggesting the importance of NMDA receptors in driving inhibitory interneuron activity

[31]. Indeed, after pharmacological blockade of NMDA receptors, gamma power in vCA1 of $Ucp2^{MGKO}$ mice increased to the level of control mice. This result aligns with findings of enhanced spontaneous hippocampal gamma oscillation in mice with selective ablation of NMDA receptors located onto PV+ interneurons [32]. In addition, our analysis of higher mIPSC in vCA1 neurons of $Ucp2^{MGKO}$ mice further corroborates alteration in inhibition.

A recent study showed that microglia can suppress neuronal activity in response to extracellular ATP released upon neuronal activation. This negative feedback mechanism is region-specific and likely functions similarly to inhibitory neurons to constrain excessive excitation in the brain [33]. Our findings of microglial impact on shaping inhibitory output in neural circuitry by spine synapse regulation extend this notion indicating that these two microglia-driven mechanisms might cooperate synergistically to maintain excitatory/inhibitory balance within neural networks. In this process, $Ucp2$ plays a key role at least in the ventral hippocampus.

Using a test battery of specific behavioral paradigms relevant to hippocampal functions, $Ucp2^{MGKO}$ male mice showed heightened anxiety levels when comparing to control animals. However, this alteration was not found in female knock-out mice. Interestingly, testing in other behavioral tasks preferentially depending on dCA1 function, such as novel object recognition, marble burying, and $Y$ maze did not reveal any obvious alteration between $Ucp2^{MGKO}$ and control animals of either gender. Overall, these results are in accordance with findings of dysfunctional neural oscillations and plasticity restricted to the vCA1. The hippocampal vCA1 with its direct projections to the prefrontal cortex and further to the basolateral amygdala are involved in the regulation of various emotional states including anxiety-like behavior [34, 35]. An intrinsic deficit in gamma oscillatory activity, as observed in $Ucp2^{MGKO}$ male mice, may lead to functional disconnections between these regions causing abnormal behavior outcomes, such as pathological anxiety. In fact, it has been shown that these three regions function as distributed networks with a high degree of interdependence, and disruption of any element within the network can cause a breakdown in their oscillatory communication and integration, thus affecting anxiety behavior [36–39].

Gamma oscillation is one of the fundamental oscillatory patterns in the hippocampal and cortical networks that support complex information processing during sensory perception, emotion regulation, attention, learning, and memory formation [40, 41]. Its alteration has been consistently detected in various diseases with impaired affective behavior and/or cognition such as generalized anxiety, attention deficit-hyperactivity disorder, schizophrenia, autism, and Alzheimer's disease

[42, 43]. Although in these psychopathological brain states different genetic and epigenetic factors were implicated in gamma oscillation abnormalities, the microglial maladaptation-induced gamma deficit such as observed here has not been reported thus far. Given the prime role of microglia in response to neural infection and injury, this effect might be highly relevant if these cells adopt an aberrant activation profile as a consequence of brain disease [44]. It is conceivable that such disease-altered microglia would exert an impact on higher brain functions. This can have particular importance in the context of acute diseases caused by pathogens with neurotropic and neuroinvasive properties, which by changing microglial functioning may contribute to the development of secondary neuropsychiatric symptoms. One such example might be viral infection with severe acute respiratory syndrome coronavirus 2 (SARS-CoV-2) which has the neuroinvasive capacity [45], can induce microglial response [46], and is linked to new-onset neurological and psychiatric symptoms in some affected subjects [47, 48].

In this study, we observed sex-related disparity in $Ucp2^{MGKO}$ mice with female mice spared from alterations in network function and behavior. Although these differences may be attributed to divergent effects of steroid hormones on neuronal and microglial functions [49], there might be other factors that require detailed analysis in the future.

In summary, we provide evidence of chronotypical and $Ucp2$-mediated crosstalk between microglia and neurons that are involved in the region-specific regulation of hippocampal function and anxiety-like behaviors. This previously unrecognized role of $Ucp2$ in maintaining complex behaviors through microglial fitness in the adult brain may open new perspectives for the discovery of novel treatments for psychiatric and neurodegenerative disorders.

**Author contributions** YY and TLH generated the concept for the study. YY, MS, MS-P, X-BG carried out experiments and analyzed data. JDK and SD provided the animal model. YY, MS, and TLH wrote the paper with input from all authors.

## Compliance with ethical standards

**Conflict of interest** The authors declare no competing interests.

# References

1. Sild M, Ruthazer ES, Booij L. Major depressive disorder and anxiety disorders from the glial perspective: Etiological mechanisms, intervention and monitoring. Neurosci Biobehav Rev. 2017;83:474–88.

2. Li Q, Barres BA. Microglia and macrophages in brain homeostasis and disease. Nat Rev Immunol. 2018;18:225–42.

3. Chu Y, Jin X, Parada I, Pesic A, Stevens B, Barres B, et al. Enhanced synaptic connectivity and epilepsy in C1q knockout mice. Proc Natl Acad Sci USA. 2010;107:7975–80.

4. Nguyen PT, Dorman LC, Pan S, Vainchtein ID, Han RT, Nakao-Inoue H, et al. Microglial remodeling of the extracellular matrix promotes synapse plasticity. Cell 2020;182:388–403 e15.

5. Blinzinger K, Kreutzberg G. Displacement of synaptic terminals from regenerating motoneurons by microglial cells. Z Zellforsch Mikros Anat. 1968;85:145–57.

6. Mondelli V, Vernon AC, Turkheimer F, Dazzan P, Pariante CM. Brain microglia in psychiatric disorders. Lancet Psychiatry. 2017;4:563–72.

7. Tejera D, Heneka MT. Microglia in neurodegenerative disorders. Methods Mol Biol. 2019;2034:57–67.

8. Trankner D, Boulet A, Peden E, Focht R, Van Deren D, Capecchi M. A microglia sublineage protects from sex-linked anxiety symptoms and obsessive compulsion. Cell Rep. 2019;29:791–99 e3.

9. Andrews ZB, Liu ZW, Walllingford N, Erion DM, Borok E, Friedman JM, et al. UCP2 mediates ghrelin's action on NPY/AgRP neurons by lowering free radicals. Nature 2008;454:846–51.

10. Paradis E, Clavel S, Bouillaud F, Ricquier D, Richard D. Uncoupling protein 2: a novel player in neuroprotection. Trends Mol Med. 2003;9:522–5.

11. Kim JD, Yoon NA, Jin S, Diano S. Microglial UCP2 mediates inflammation and obesity induced by high-fat feeding. Cell Metab. 2019;30:952–62 e5.

12. Anacker C, Hen R. Adult hippocampal neurogenesis and cognitive flexibility—linking memory and mood. Nat Rev Neurosci. 2017;18:335–46.

13. Grabert K, Michoel T, Karavolos MH, Clohisey S, Baillie JK, Stevens MP, et al. Microglial brain region-dependent diversity and selective regional sensitivities to aging. Nat Neurosci. 2016;19:504–16.

14. Attardo A, Fitzgerald JE, Schnitzer MJ. Impermanence of dendritic spines in live adult CA1 hippocampus. Nature 2015;523:592–6.

15. Diano S, Farr SA, Benoit SC, McNay EC, da Silva I, Horvath B, et al. Ghrelin controls hippocampal spine synapse density and memory performance. Nat Neurosci. 2006;9:381–8.

16. Franklin KBJ, Paxinos G. Paxinos and Franklin's the mouse brain in stereotaxic coordinatesl. Fourth edn. Amsterdam: Academic Press (an imprint of Elsevier). 2013.

17. Rao Y, Mineur YS, Gan G, Wang AH, Liu ZW, Wu X, et al. Repeated in vivo exposure of cocaine induces long-lasting synaptic plasticity in hypocretin/orexin-producing neurons in the lateral hypothalamus in mice. J Physiol. 2013;591:1951–66.

18. Tucker LB, McCabe JT. Behavior of male and female C57BL/6J mice is more consistent with repeated trials in the elevated zero maze than in the elevated plus maze. Front Behav Neurosci. 2017;11:13.

19. Gould TD, Dao DT, Kovacsics CE. The open field test. In: Mood and anxiety related phenotypes in mice. 2009, pp 1–20.

20. Antunes M, Biala G. The novel object recognition memory: neurobiology, test procedure, and its modifications. Cogn Process. 2012;13:93–110.

21. Leger M, Quiedeville A, Bouet V, Haelewyn B, Boulouard M, Schumann-Bard P, et al. Object recognition test in mice. Nat Protoc. 2013;8:2531–7.

22. Deacon RM. Digging and marble burying in mice: simple methods for in vivo identification of biological impacts. Nat Protoc. 2006;1:122–4.

23. Adeosun SO, Hou X, Zheng B, Stockmeier C, Ou X, Paul I, et al. Cognitive deficits and disruption of neurogenesis in a mouse model of apolipoprotein E4 domain interaction. J Biol Chem. 2014;289:2946–59.

24. Iyer R, Wang TA, Gillette MU. Circadian gating of neuronal functionality: a basis for iterative metaplasticity. Front Syst Neurosci. 2014;8:164.

25. Abraham WC. Metaplasticity: tuning synapses and networks for plasticity. Nat Rev Neurosci. 2008;9:387.

26. Park D, Han CZ, Elliott MR, Kinchen JM, Trampont PC, Das S, et al. Continued clearance of apoptotic cells critically depends on the phagocyte Ucp2 protein. Nature. 2011;477:220–4.

27. Marschallinger J, Iram T, Zardeneta M, Lee SE, Lehallier B, Haney MS, et al. Lipid-droplet-accumulating microglia represent a dysfunctional and proinflammatory state in the aging brain. Nat Neurosci. 2020;23:194–208.

28. Uhlhaas PJ, Singer W. Abnormal neural oscillations and synchrony in schizophrenia. Nat Rev Neurosci. 2010;11:100–13.

29. Gonzalez-Burgos G, Lewis DA. NMDA receptor hypofunction, parvalbumin-positive neurons, and cortical gamma oscillations in schizophrenia. Schizophr Bull. 2012;38:950–7.

30. Berry KP, Nedivi E. Spine dynamics: are they all the same? Neuron. 2017;96:43–55.

31. Rotaru DC, Yoshino H, Lewis DA, Ermentrout GB, Gonzalez-Burgos G. Glutamate receptor subtypes mediating synaptic activation of prefrontal cortex neurons: relevance for schizophrenia. J Neurosci. 2011;31:142–56.

32. Korotkova T, Fuchs EC, Ponomarenko A, von Engelhardt J, Monyer H. NMDA receptor ablation on parvalbumin-positive interneurons impairs hippocampal synchrony, spatial representations, and working memory. Neuron. 2010;68:557–69.

33. Badimon A, Strasburger HJ, Ayata P, Chen X, Nair A, Ikegami A, et al. Negative feedback control of neuronal activity by microglia. Nature. 2020;586:417–23.

34. Godsil BP, Kiss JP, Spedding M, Jay TM. The hippocampal-prefrontal pathway: the weak link in psychiatric disorders? Eur Neuropsychopharmacol. 2013;23:1165–81.

35. Hare BD, Duman RS. Prefrontal cortex circuits in depression and anxiety: contribution of discrete neuronal populations and target regions. Mol Psychiatry. 2020;25:2742–58.

36. Bannerman DM, Grubb M, Deacon RM, Yee BK, Feldon J, Rawlins JN. Ventral hippocampal lesions affect anxiety but not spatial learning. Behav Brain Res. 2003;139:197–213.

37. Adhikari A, Topiwala MA, Gordon JA. Single units in the medial prefrontal cortex with anxiety-related firing patterns are preferentially influenced by ventral hippocampal activity. Neuron. 2011;71:898–910.

38. Likhtik E, Stujenske JM, Topiwala MA, Harris AZ, Gordon JA. Prefrontal entrainment of amygdala activity signals safety in learned fear and innate anxiety. Nat Neurosci. 2014;17:106–13.

39. Padilla-Coreano N, Bolkan SS, Pierce GM, Blackman DR, Hardin WD, Garcia-Garcia AL, et al. Direct ventral hippocampal-prefrontal input is required for anxiety-related neural activity and behavior. Neuron. 2016;89:857–66.

40. Fries P. Neuronal gamma-band synchronization as a fundamental process in cortical computation. Annu Rev Neurosci. 2009;32:209–24.

41. Headley DB, Pare D. In sync: gamma oscillations and emotional memory. Front Behav Neurosci. 2013;7:170.

42. Uhlhaas PJ, Singer W. Neural synchrony in brain disorders: relevance for cognitive dysfunctions and pathophysiology. Neuron. 2006;52:155–68.

43. Mably AJ, Colgin LL. Gamma oscillations in cognitive disorders. Curr Opin Neurobiol. 2018;52:182–87.

44. Butovsky O, Weiner HL. Microglial signatures and their role in health and disease. Nat Rev Neurosci. 2018;19:622–35.

45. Song E, Zhang C, Israelow B, Lu-Culligan A, Prado AV, Skria-bine S, et al. Neuroinvasion of SARS-CoV-2 in human and mouse brain. J Exp Med. 2021;218:e20202135. https://doi.org/10.1084/jem.20202135.

46. Matschke J, Lutgehetmann M, Hagel C, Sperhake JP, Schroder AS, Edler C, et al. Neuropathology of patients with COVID-19 in Germany: a post-mortem case series. Lancet Neurol. 2020;19:919–29.

47. Varatharaj A, Thomas N, Ellul MA, Davies NWS, Pollak TA, Tenorio EL, et al. Neurological and neuropsychiatric complications of COVID-19 in 153 patients: a UK-wide surveillance study. Lancet Psychiatry. 2020;7:875–82.

48. Rogers JP, Chesney E, Oliver D, Pollak TA, McGuire P, Fusar-Poli P, et al. Psychiatric and neuropsychiatric presentations associated with severe coronavirus infections: a systematic review and meta-analysis with comparison to the COVID-19 pandemic. Lancet Psychiatry. 2020;7:611–27.

49. Kokkosis AG, Tsirka SE. Neuroimmune mechanisms and sex/gender-dependent effects in the pathophysiology of mental disorders. J Pharm Exp Ther. 2020;375:175–92.